

PSFC/JA-01-15

Simulation of Photonic Band Gaps in Metal  
Rod Lattices for Microwave Applications

E. I. Smirnova, C. Chen, M. A. Shapiro and R. J. Temkin

July 2001

Plasma Science and Fusion Center  
Massachusetts Institute of Technology  
Cambridge, MA 02139, USA

This work was supported by the Department of Defense under the MURI Innovative Microwave Vacuum Electronics Program, 1999, and in part by the Department of Energy, office of High Energy and Nuclear Physics and the Air Force Office of Scientific Research, Grant No. F49620-00-1-0007. Reproduction, translation, publication, use and disposal, in whole or part, by or for the United States government is permitted.

Submitted for publication in *Journal of Applied Physics*.

# **SIMULATION OF PHOTONIC BAND GAPS IN METAL ROD LATTICES FOR MICROWAVE APPLICATIONS**

E. I. Smirnova, C. Chen, M.A. Shapiro, J.R. Sirigiri, and R.J. Temkin  
Plasma Science and Fusion Center  
Massachusetts Institute of Technology  
Cambridge, MA 02139

## **ABSTRACT**

We have derived the global band gaps for general two-dimensional (2D) photonic band gap (PBG) structures formed by square or triangular arrays of metal posts. Such PBG structures have many promising applications in active and passive devices at microwave, millimeter wave and higher frequencies. A coordinate-space, finite-difference code, called the photonic band gap structure simulator (PBGSS), was developed to calculate complete dispersion curves for lattices for a series of values of the ratio of the post radius ( $a$ ) to the post spacing ( $b$ ). The fundamental and higher frequency global photonic band gaps were determined numerically. These universal curves should prove useful in PBG cavity design. In addition, for very long wavelengths, where the numerical methods of the PBGSS code are difficult, dispersion curves were derived for the TM mode by an approximate, quasi-static approach. Results of this approach agree well with the PBGSS code for  $a/b < 0.1$ . The present results are compared with experimental data for TE and TM mode PBG resonators built at MIT and the agreement is found to be very good.

PACS: 42. 70. Qs; 41.20.Jb.

## I. INTRODUCTION

In high-power microwave devices, the interaction of an intense electron beam with rf circuit is employed. In highly overmoded resonators of devices such as gyrotrons, the problem of mode competition arises. To obtain high-efficiency, single-mode excitation of microwaves, the rf circuit must be selective with respect to the operating mode, and the unwanted oscillations must be suppressed. The use of photonic band gap (PBG) structures [1], and in particular 2D PBG structures [2], has been experimentally shown to be a promising approach to the realization of mode selective circuits [3-8].

The intensive PBG structure research originated from studying of dielectric lattices [1,2,9-11]. Recently, considerable interest in metallic PBG structures [5-8,12-14] has been expressed. For analysis of metallic PBG cavities formed by single or multiple defects in the PBG structure, finite-element codes such as SUPERFISH [15] and HFSS [16] are ideally suited. For studies of wave propagation in the bulk of metallic PBG structures, on the other hand, the plane wave expansion method [12], generalized Rayleigh expansion method [13], finite-difference time-domain scheme [14] and the coordinate-space finite-difference method [5] have been used. It is well known [12] that due to the convergence problem, the plane wave expansion method is applicable only to the lattices with the size of conductors small compared with the lattice period, but at microwave frequencies the lattices with a large ratio of post radius to the lattice constant are of the main interest [5-8].

One of the most important and computationally challenging problems is the calculation of the global photonic band gaps. A number of papers [2,10,11] report that the global photonic band gaps were determined for dielectric lattices. An attempt to study global photonic band gaps in metallic lattices was made in [13], but only the first-order band gap of a square lattice was calculated there.

In this paper, we present the results of the numerical and theoretical investigation of the wave propagation in 2D perfect conductor (metal) lattices. Using the coordinate-space finite-difference method, we have developed a code, named Photonic Band Gap Structure Simulator (PBGSS) [17], to analyze the dispersion characteristics for the wave propagation in the bulk of 2D square and triangular PBG structures. The coordinate-space finite-difference method is used in PBGSS because of its reliability and high accuracy

with fine grids. Extensive numerical simulations were performed to determine the fundamental and higher frequency global photonic band gaps for both TE and TM modes in square and triangular lattices. In our calculation we put the longitudinal wave vector equal to zero that obviously does not affect the generosity of results. The global band gap charts are extremely useful for the design of PBG devices such as metallic PBG cavities with high mode selectivity. In addition, some theoretical quasistatic estimates for the TM mode dispersion curves in square lattices are proposed, and these estimates are in good agreement with the PBGSS simulations for the case of the conducting post size much smaller than the wavelength. Finally, comparisons are made between the PBGSS simulations and several recent experiments [7,8].

The organization of this article is as follows. In Sec. II, we describe the numerical method employed in the PBGSS code. In Sec. III, we present the results of dispersion curves and global photonic band gap calculations. In Sec. IV, the comparison is made between the PBGSS simulations for the case of the small post radius and theoretical quasistatic estimates. In Sec. V, we compare the results of PBGSS simulation and several experiments performed recently at MIT. Conclusions are presented in Section VI.

## II. FINITE-DIFFERENCE ALGORITHM DESCRIPTION

Two types of metal lattices are considered, namely the square lattice [Fig. 1(a)] and the triangular lattice [Fig. 1(b)]. The system of a 2D periodic array of metal cylinders is fully described by the periodic conductivity profile, which for the case of a square lattice is

$$\sigma(\mathbf{x}) = \sigma(\mathbf{x}_\perp) = \begin{cases} \infty, & (x - mb)^2 + (y - nb)^2 < a^2, \\ 0, & \text{otherwise,} \end{cases} \quad (1)$$

and for the triangular lattice is given by

$$\sigma(\mathbf{x}) = \sigma(\mathbf{x}_\perp) = \begin{cases} \infty, & \left[ x - \left( m + \frac{n}{2} \right) b \right]^2 + \left[ y - \frac{\sqrt{3}}{2} nb \right]^2 < a^2, \\ 0, & \text{otherwise.} \end{cases} \quad (2)$$

In (1) and (2),  $\mathbf{x}_\perp = x\hat{\mathbf{e}}_x + y\hat{\mathbf{e}}_y$  is the transverse displacement,  $a$  is the radius of the conducting cylinder,  $b$  is the lattice spacing, and  $m$  and  $n$  are integers. The conductivity profile satisfies the periodic condition

$$\sigma(\mathbf{x}_\perp + \mathbf{T}_{mn}) = \sigma(\mathbf{x}_\perp), \quad (3)$$

with the set of periodicity vectors  $\mathbf{T}_{mn}$  defined as

$$\mathbf{T}_{mn} = \begin{cases} m b \hat{\mathbf{e}}_x + n b \hat{\mathbf{e}}_y & \text{(square lattice),} \\ \left( m + \frac{n}{2} \right) b \hat{\mathbf{e}}_x + \frac{\sqrt{3}}{2} n b \hat{\mathbf{e}}_y & \text{(triangular lattice).} \end{cases} \quad (4)$$

### A. Formulation of the Eigenvalue Problem

It is readily shown from Maxwell's equations that the wave field in the two-dimensional PBG structures can be decomposed into two independent classes of modes: the transverse electric (TE) modes and the transverse magnetic (TM) modes. In a TE mode the electric field vector is perpendicular to the post axis and in a TM mode the magnetic field vector is perpendicular to the post axis. All the field components in the TM (TE) modes can be expressed through the axial component of the electric (magnetic) field, which we will further denote by  $\psi$ . Since the system is homogeneous along the  $z$ -axis, we can take the Fourier transform of  $\psi$  in axial coordinate  $z$  and time  $t$  and consider

$$\psi(\mathbf{x}_\perp, k_z, \omega) = \iint \psi(\mathbf{x}_\perp, z, t) e^{i(k_z z - \omega t)} dz dt,$$

which we will denote hereafter by  $\psi(\mathbf{x}_\perp)$  assuming that the frequency  $\omega$  and the longitudinal wave number  $k_z$  are fixed. The Helmholtz equation for  $\psi(\mathbf{x}_\perp)$  follows from Maxwell's equations,

$$\nabla_\perp^2 \psi(\mathbf{x}_\perp) = \left( k_z^2 - \frac{\omega^2}{c^2} \right) \psi(\mathbf{x}_\perp). \quad (5)$$

The boundary conditions on the surfaces  $S$  of the conducting posts are

$$\psi|_S = 0 \quad (\text{TM mode}), \quad (6)$$

$$\frac{\partial \psi}{\partial \mathbf{n}} \Big|_S = 0 \quad (\text{TE mode}), \quad (7)$$

where  $\mathbf{n}$  is the normal vector to the post surface.

The discrete translational symmetry of the conductivity profile allows us to write the fundamental solution of the Helmholtz equation in Bloch form so that

$$\psi(\mathbf{x}_\perp + \mathbf{T}) = \psi(\mathbf{x}_\perp) e^{i\mathbf{k}_\perp \cdot \mathbf{T}}, \quad (8)$$

where  $\mathbf{T}$  is any vector of  $\mathbf{T}_{mn}$ ,  $\mathbf{k}_\perp = k_x \hat{\mathbf{e}}_x + k_y \hat{\mathbf{e}}_y$  is an arbitrary transverse wave number.

Thus we need only solve (5) inside the fundamental unit cell defined by

$$|x| \leq b/2, \quad |y| \leq b/2 \quad (\text{square lattice}), \quad (9)$$

$$\left| x - \frac{y}{\sqrt{3}} \right| \leq \frac{b}{2}, \quad |y| \leq \frac{\sqrt{3}}{4} b \quad (\text{triangular lattice}). \quad (10)$$

The following periodic boundary conditions are deduced from (8)

$$\begin{cases} \psi\left(-\frac{b}{2}, y\right) = e^{ik_x b} \psi\left(\frac{b}{2}, y\right) \\ \psi\left(x, -\frac{b}{2}\right) = e^{ik_y b} \psi\left(x, \frac{b}{2}\right) \end{cases} \quad (\text{square lattice}), \quad (11)$$

$$\begin{cases} \psi\left(-\frac{b}{2}, y\right) = e^{ik_x b} \psi\left(\frac{b}{2}, y\right) \\ \psi\left(x, \frac{\sqrt{3}}{4} b\right) = e^{ik_x \frac{b}{2} + ik_y \frac{\sqrt{3}b}{2}} \psi\left(x - \frac{b}{2}, -\frac{\sqrt{3}}{4} b\right) \end{cases} \quad (\text{triangular lattice}), \quad (12)$$

Equation (5) together with boundary conditions (6) and (11) or (7) and (12) define the eigenvalue problem of finding  $\lambda^2 = \omega^2 / c^2 - k_z^2$  as a function of  $\mathbf{k}_\perp$ .

The periodicity of the exponent in (8) means that the possible values  $\mathbf{k}_\perp$  can be restricted to the irreducible Brillouin zones of the reciprocal lattices, which for the cases of square and triangular lattices are illustrated in Fig. 2. The three special points in Fig.

2(a)  $\Gamma$ , X and M correspond respectively to  $\mathbf{k}_\perp = 0$ ,  $\mathbf{k}_\perp = \frac{\pi}{b}\hat{\mathbf{e}}_x$  and  $\mathbf{k}_\perp = \frac{\pi}{b}(\hat{\mathbf{e}}_x + \hat{\mathbf{e}}_y)$ .

The three special points in Fig. 2(b)  $\Gamma$ , X and J correspond to  $\mathbf{k}_\perp = 0$ ,  $\mathbf{k}_\perp = \frac{2\pi}{\sqrt{3}b}\hat{\mathbf{e}}_y$  and

$$\mathbf{k}_\perp = \frac{2\pi}{3b}(\hat{\mathbf{e}}_x + \sqrt{3}\hat{\mathbf{e}}_y).$$

## B. Numerical Scheme of the Eigenvalue Computation

To compute the eigenmodes for rf wave propagation in the two-dimensional PBG structures, we have developed a Photonic Band Gap Structure Simulator (PBGSS) code [17]. The PBGSS code is based on a real-space finite difference method. We cover the fundamental unit cell of the square (triangular) lattice by square (triangular) mesh with  $(2N+1)\times(2N+1)$  mesh points. Outside the conducting posts, the Helmholtz equation (5) is approximated by the set of linear relations between the values  $\psi_{i,j}$  of the function  $\psi(\mathbf{x}_\perp)$  at the point  $(i, j)$  of the mesh (the mesh point  $i = j = 0$  corresponds to the origin of the fundamental cell). We will refer to the equation

$$\psi_{i+1,j} + \psi_{i-1,j} + \psi_{i,j+1} + \psi_{i,j-1} - 4\psi_{i,j} = -\lambda^2 h^2 \psi_{i,j} \quad (13)$$

for the square lattice, and

$$4(\psi_{i+1,j} + \psi_{i-1,j} + \psi_{i,j+1} + \psi_{i,j-1}) - (\psi_{i+1,j+1} - \psi_{i+1,j-1} - \psi_{i-1,j+1} + \psi_{i-1,j-1}) - 16\psi_{i,j} = -3\lambda^2 h^2 \psi_{i,j} \quad (14)$$

for the triangular lattice, as “equation  $(i, j)$ ”. Here  $h = b/(2N+1)$  is the mesh step. The periodic boundary conditions (11) and (12) are expressed explicitly as

$$\psi_{N+1,j} = \psi_{-N,j} e^{ik_x b}, \quad \psi_{i,N+1} = \psi_{i,-N} e^{ik_y b} \quad (\text{square lattice}), \quad (15)$$

$$\psi_{N+1,j} = \psi_{-N,j} e^{ik_x b}, \quad \psi_{i,N+1} = \psi_{i,-N} e^{i\frac{b}{2}(k_x + \sqrt{3}k_y)} \quad (\text{triangular lattice}). \quad (16)$$

The mesh points, which fall inside the conducting posts, are excluded from the system of linear equations (13) or (14) using boundary conditions (6) or (7). The boundary

condition in (6) is implemented by setting the value of  $\psi_{i,j} = 0$  for the grid point  $(i, j)$  inside of the conducting cylinder. The boundary condition (7) is implemented in the following way: if some point entering the linear equation  $(i, j)$  falls inside the post we put the value of  $\psi$  in this point equal to  $\psi_{i,j}$ . This approximation seems to be crude, but we have chosen the simplest implementation of the boundary conditions in order to preserve the Hermitian nature of the matrix of linear equations (13) or (14). Since we do not take into account the losses in electrodynamic system, the initial eigenvalue problem is Hermitian, and we have found empirically that the preservation of the Hermitian nature improved the convergence of the algorithm. Thus we obtain a closed set of  $(2N + 1)^2 - M$  linear equations, where  $M$  is the number of the mesh points that fall inside the conducting cylinder. The matrix of this system is Hermitian and we compute the eigenvalues  $\lambda$  from a standard Fortran subroutine.



### III. RESULTS OF EIGENMODE AND BAND GAPS CALCULATIONS

In this section, we present the new results of PBGSS calculations of the eigenfrequencies for TE and TM modes in the two-dimensional square and triangular lattices. Initial results of the PBGSS calculations were discussed elsewhere [17]. For all the plots presented we set  $k_z = 0$ , which obviously does not affect the generality of the results. In all the PBGSS calculations, we use the value of  $N = 20$ . Our experience shows that the results are nearly identical as  $N$  is further increased.

#### A. TM Modes

Figure 3 is presented to demonstrate the local band gap, which occurs at the X point [see Fig. 2] of the Brillouin zone, as obtained from the PBGSS calculations for  $a/b = 0.2$ . Figure 3(a) shows the first and second TM propagating modes (simply referred to below as “modes”) in the square lattice, where the band gap is actually the result of the interaction of two waves with  $\mathbf{k}_1 = \frac{\pi}{b}\hat{\mathbf{e}}_x$  and  $\mathbf{k}_2 = -\frac{\pi}{b}\hat{\mathbf{e}}_x$  in the periodic structure. Figure 3(b) shows the first and second TM modes in the triangular lattice.

Figure 4 shows the dispersion characteristics (Brillouin diagrams) for the TM modes as the wave vector  $\mathbf{k}_\perp$  varies from the center of the Brillouin zone ( $\Gamma$  point in Fig. 2), to the nearest edge of the Brillouin zone (X point in Fig. 2), and to the far edge of the Brillouin zone (M point for the square lattice and J point for the triangular lattice). Two cases correspond to different types of lattices. In Fig. 4,  $a/b = 0.2$  and for the square lattice a global band gap between the first and second modes can be seen. For the triangular lattice the first and the second mode are intersecting and there is no band gap between them. For the TM modes, there is a cut-off frequency that is the zeroth-order band gap.

To determine the global TM band gaps, we perform more extensive computations. It is important to perform simulations with small grid step to assure the accuracy of the simulation results. For each value of  $a/b$ , we search through all  $\mathbf{k}_\perp$  on the boundary of the Brillouin zone and find the minimum and maximum of each dispersion curve. Then we check if there is a gap between any two adjacent modes, i.e., if the minimum of the higher order mode is above the maximum of the lower order mode. The results are shown

in Fig. 5. Shown in Fig. 5(a) are the five lowest-order global TM band gaps for the square lattice. The zeroth-order global TM band gap exists below the first mode, that is, there is a cutoff frequency for the TM modes. The cutoff frequency exists even for very small conducting cylinders and goes to zero logarithmically as  $a/b \rightarrow 0$  (which is illustrated in Fig. 5 with a dashed curve continuation of the calculated cutoff curve). The first-order global TM band gap occurs between the first and second lowest modes. There is a threshold for first-order global TM band gap opening at  $a/b \cong 0.1$ . Higher-order global TM band gaps occur between the third and fourth, fourth and fifth, and fifth and sixth modes. There is no global band gap between the second and third modes.

Shown in Fig. 5(b) there are three lowest-order global TM band gaps for the triangular lattice. In Fig. 5(b), the zeroth-order global TM band gap exists below the first mode, which is similar to the case of the square lattice. Though there is a local band gap at X point between the first and second modes (as shown in Fig. 3), these modes are intersecting at J point and the global band gap does not occur between them. The threshold for the occurrence of the first-order global TM band gap, which is between the second and third modes, is  $a/b \cong 0.2$ . The second-order global TM band gap occurs between the sixth and seventh modes. We find that the width of each global TM band gap increases as the ratio  $a/b$  increases.

## B. TE Modes

Figure 6 shows the TE mode local band gap, which occurs at the X point [see Fig. 2] of the Brillouin zone, as obtained from the PBGSS calculations. Figure 6(a) demonstrates the dispersion curves for the first and second TE propagating bands in the square lattice. Figure 6(b) shows the dispersion curves for the first and second TE propagating bands in the triangular lattice. In contrast to the TM mode, there is no cutoff in the case of a TE mode. The first mode goes to zero at the  $\Gamma$  point for both square and triangular lattices. The first mode at the  $\Gamma$  point degenerates into the electrostatic static solution (with zero frequency), which satisfies the boundary conditions (6).

Figure 7 shows the Brillouin diagrams for the TE modes as the wave vector  $\mathbf{k}_\perp$  varies from the center of the Brillouin zone ( $\Gamma$  point in Fig. 2), to the nearest edge of the Brillouin zone (X point in Fig. 2), and to the far edge of the Brillouin zone (M point for

the square lattice and J point for the triangular lattice). Two cases correspond to the square and triangular lattices. In Fig. 7,  $a/b = 0.2$  and there are no global TE band gaps for either square or triangular lattices. This is different from the TM case where the first band gap occurs between the first and second modes for  $a/b \geq 0.1$ .

We have also calculated the global TE band gaps in both types of lattices. The results are shown in Fig. 8. For the square lattice (Fig. 8(a)), we found that the first global TE band gap occurs when  $a/b > 0.3$ . This is the band gap between the first and second modes, which are tangent at the M point for lower ratios of  $a/b$ . Unlike the first global TM band gap, the lower boundary of this band gap decreases with increasing  $a/b$ . The higher order band gap opens and then closes for even lower ratio of  $a/b$ , this gap is between the sixth and the seventh modes.

For the triangular lattice three lowest global TE band gaps are shown in Fig. 8(b). All of these gaps tend to close with increasing  $a/b$  except for the lowest one, which occurs between the second and third modes for  $a/b > 0.35$ . The second global TE band gap, which is between the third and fourth modes, appears for lower ratios of  $a/b$  than those for the lowest global TE band gap. The third global TE band gap is between the sixth and seventh modes.

The global TE band gaps in the metallic lattice resemble qualitatively the previously reported global TE and TM band gaps in dielectric lattices [2,11], which typically close with increasing  $a/b$ . But there are two striking differences between the metal bandgaps and dielectric band gaps. First, there is a zeroth-order global TM band gap in metallic lattices, which is a cutoff analogous to that in a conventional waveguide and exists for all values of  $a/b$ , whereas there is no such cutoff in dielectric lattices for either TE or TM modes. Second, the width of the global TM band gap in the metallic lattice increases with increasing  $a/b$ , whereas the global TE and TM band gaps in dielectric lattices typically close as the ratio  $a/b$  increases.

#### IV. COMPARISON BETWEEN PBGSS SIMULATION AND QUASISTATIC APPROXIMATION

While trying to benchmark theoretically the PBGSS calculations, we found an explanation of the behavior of the first and second dispersion curves for the TM mode near the X point in a square lattice in the framework of the quasistatic approximation, which we described in this section. As mentioned earlier, the X point in a square lattice corresponds to a simple case of the wave propagation in the  $x$ -direction with  $k_y = k_z = 0$ .

Fig. 9(a) shows two rows of the posts with a wave incident perpendicularly. The electric field in the wave is parallel to the posts and excites longitudinal currents in them. The alternating current radiates and so a reflection appears. The reflections from different rows if phased properly can cause the total reflection of the wave from the PBG array, and that is how the local bandgap forms.

Instead of describing the electromagnetic system in terms of the fields  $\mathbf{E}$  and  $\mathbf{H}$  it is convenient to introduce new variables: the ‘source voltage’  $V$  and ‘current’  $I$  per unit length of the post. The ‘voltage’ and ‘current’ are measures of the lowest mode electric field parallel to the posts and the lowest mode magnetic field transverse to the posts. The voltages and currents obey the transmission line equations since the fields themselves obey such equations. From this point of view one row of the posts can be properly described by an equivalent two-port circuit, in which the conducting cylinders are represented by lumped elements [19]. The equivalent circuit is illustrated in Fig. 9(b). The following values of impedances  $X_a$  and  $X_b$ , valid in the limit  $a\omega/2\pi c \ll 1$  and  $a/b \ll 1$  are given in [19]:

$$X_a = Z_0 \frac{\Omega}{2\pi} \left\{ \ln \left( \frac{b}{2\pi a} \right) + \sum_{m=1}^{\infty} \left[ \left( m^2 - \frac{\Omega^2}{4\pi^2} \right)^{-1/2} - \frac{1}{m} \right] \right\}, \quad (17)$$

$$X_b = 2\pi Z_0 \Omega \left( \frac{a}{b} \right)^2, \quad (18)$$

where  $Z_0 = 377$  ohm is the impedance of vacuum and  $\Omega = \omega b/c$  is the normalized frequency. Because we consider a lossless system, all the reactances and susceptances in Fig. 9(b) are purely imaginary. It should be emphasized, that it is only the sign of a reactance or susceptance that dictates whether an inductor or capacitor is chosen. The

reactance or susceptance does not, in general, have the simple frequency dependence of a lumped-element inductor or capacitor. Since the row of posts has a plane of symmetry, the two capacitors in the circuit can be chosen of equivalent value.

Suppose, we apply a current source  $I_1$  at port 1 in Fig. 9(b) and current source  $I_2$  at port 2. Let  $V_{ij}$  be the voltage at port  $i$  due to the source  $I_j$ . The impedance matrix  $\hat{Z}$  is introduced with the elements representing the various reactions between two current sources

$$\hat{Z} = \begin{pmatrix} Z_{11} & Z_{12} \\ Z_{21} & Z_{22} \end{pmatrix}, \quad Z_{ij} = \frac{V_{ij}}{I_j}.$$

Using the Kirchhoff laws we find the elements of matrix  $\hat{Z}$

$$Z_{11} = Z_{22} = -iX_a + iX_b, \quad (19)$$

$$Z_{12} = Z_{21} = -iX_a, \quad (20)$$

The transmission matrix  $\hat{T}$  relates the voltage and current at port 2 to the voltage and current at port 1

$$\begin{pmatrix} V_2 \\ I_2 \end{pmatrix} = \hat{T} \begin{pmatrix} V_1 \\ I_1 \end{pmatrix}.$$

Matrix  $\hat{T}$  is related to  $\hat{Z}$  in the following way

$$\hat{T} = \begin{pmatrix} \frac{Z_{22}}{Z_{12}} & -\frac{Z_{11}Z_{22} - Z_{12}^2}{Z_{12}} \\ \frac{1}{Z_{12}} & \frac{Z_{11}}{Z_{12}} \\ -\frac{1}{Z_{12}} & \frac{Z_{11}}{Z_{12}} \end{pmatrix}. \quad (21)$$

The square lattice, representing a conducting cylinder array is a periodic sequence of the rows separated by the distance  $b$ , and the equivalent circuit of this array is a periodic chain of two-port circuits and spacings. The electric and magnetic fields and so the voltage and current vary sinusoidally along the spacing and the fields on the right edge of the spacing are related to the voltage and current on the left edge by the spacing transmission matrix

$$\hat{T}_s = \begin{pmatrix} \cos \Omega & iZ_0 \sin \Omega \\ \frac{i}{Z_0} \sin \Omega & \cos \Omega \end{pmatrix}. \quad (22)$$

The transmission matrix of one period of the chain of rows is given by the multiplication of two transmission matrixes:

$$\hat{A} = \hat{T} \cdot \hat{T}_s. \quad (23)$$

Consider the infinite chain of rows. Let us search for the eigenmode of such a system with the effective voltage and current changing from one row to another as

$$\begin{aligned} V(nb) &= V(0)e^{ik_x bn}, \\ I(nb) &= I(0)e^{ik_x bn}. \end{aligned}$$

The voltages and currents at the adjacent rows are connected through the transmission matrix

$$\begin{pmatrix} V(b) \\ I(b) \end{pmatrix} = \begin{pmatrix} V(0) \\ I(0) \end{pmatrix} e^{ik_x b} = \hat{A} \begin{pmatrix} V(0) \\ I(0) \end{pmatrix}. \quad (24)$$

The equation (24) has a nontrivial solution only when  $\det(\hat{A} - \hat{I} e^{ik_x b}) = 0$ . This together with the transmission matrix property  $\det \hat{A} = A_{11}A_{22} - A_{21}A_{12} = 1$  finally gives us the approximate dispersion relation for TM wave propagation in the  $x$ -direction in the square lattice of thin conductors

$$\cos(k_x b) = \frac{A_{11} + A_{22}}{2} = \left(1 - \frac{X_b}{X_a}\right) \cos \Omega + \frac{1}{2} \left( \frac{2X_a X_b - X_b^2}{X_a Z_0} + \frac{Z_0}{X_a} \right) \sin \Omega. \quad (25)$$

When the perturbation is absent (i.e., when there are no metallic posts),  $k_x b = \pi$ ,  $\Omega = \pi$  is the solution of (25). In the system with posts, equation (25) will give two distinct roots for  $\Omega$  when  $k_x b = \pi$ . The difference between the two roots, denoted by  $\Delta\Omega = \Omega_2 - \Omega_1$ , gives the width of the first local gap at the X point.

For  $\Omega \approx \pi$  and  $a/b \ll 1$ , we rewrite (17) and (18) approximately as

$$X_a \cong Z_0 \frac{\Omega}{2\pi} \left\{ \ln \left( \frac{b}{2\pi a} \right) + \sum_{m=1}^{\infty} \left[ \frac{1}{\sqrt{m^2 - 1/4}} - \frac{1}{m} \right] \right\} = Z_0 \frac{\Omega}{2\pi} \left\{ \ln \left( \frac{b}{2\pi a} \right) + 0.181 \right\}, \quad (26)$$

$$X_b \cong 0. \quad (27)$$

For very low ratios of  $a/b$  such that  $\ln(b/2\pi a) \gg 1$ , the logarithmic term in Eq. (26) dominates, and equation (25) together with (26) and (27) yields at  $k_x b = \pi$

$$\begin{aligned}
\Omega_1 &= \pi + O\left(\frac{a^2}{b^2}\right), \\
\Omega_2 &= \pi + \Delta\Omega, \\
\Delta\Omega &= \frac{2}{\ln(b/2\pi a) + 0.818} + O\left(\frac{1}{(\ln(b/2\pi a))^3}\right).
\end{aligned} \tag{28}$$

To benchmark the PBGSS code, we compare the above theoretical results to the simulations. Figure 10 shows the dependence of the local TM band gap width at the X-point on the ratio  $a/b$  in the interval  $0 < a/b < 0.1$  for the square lattice. The dotted curve is obtained in the following way: we plug the expressions (17) and (18) for  $X_a$  and  $X_b$  to (25) and then solve it numerically for  $\Omega$  for  $k_x b = \pi$  and different  $a/b$ . The solid curve is obtained from PBGSS calculations. Fig. 10 indicates that the PBGSS simulation results agree with the quasi-static theory within 10%. This is consistent with the fact that the errors in the approximate expressions for the impedances (17) and (18) were estimated in [19] to be less than 10% in the range  $0 < a/b < 0.1$ . Thus we conclude that the results from the PBGSS calculations are in good agreement with the analytical result for  $a/b \ll 1$ .

## V. DESIGN OF PBG CAVITIES FOR ACCELERATOR AND MICROWAVE GENERATION EXPERIMENTS

Two PBG experiments were conducted recently at MIT. The first one was an accelerator cavity operating in the TM mode [7], and the second one was a gyrotron cavity with a TE mode [8]. These applications of the PBG cavity are to eliminate competing modes, which appear in conventional accelerator or gyrotron resonators and reduce the efficiency of the bunch acceleration or mode excitation. The SUPERFISH [15] and HFSS [16] codes were used for the PBG cavity designs. However, neither SUPERFISH nor HFSS codes can be used to calculate global band gaps in PBG cavities and thus cannot serve as a proof of the single mode excitation. The new code calculating the bulk PBG structures dispersion characteristics was needed and thus the PBGSS code was created.

The MIT PBG accelerator cavity is made up of a triangular lattice of metal rods and operates in the TM mode at 17 GHz [7]. The PBG accelerator cavity was first proposed in [6] with the accelerating TM mode formed by a defect in a 2D square metal lattice. A defect in the 17 GHz MIT accelerator cavity is created by one missing rod in a triangular lattice. The lattice has the post radius  $a = 0.079$  cm and the distance between the nearest posts  $b = 0.64$  cm, which corresponds to  $a/b = 0.123$  and  $\omega b/c = 2.28$ . The operational point of the cavity is shown by the solid dot in the Fig. 5(b). It can be seen from the picture that the cavity operates in the zero-order band gap (below the cutoff) and there are no other band gaps above. This proves that there is only one mode, which can be confined in the cavity. The higher frequency modes excited by the electron bunch in conventional accelerator (wakefields) are able to leak through the lattice, which provides an effective damping mechanism for the wakefields in the cavity. Fig. 11(a) shows the cross-section of the HFSS model of the PBG accelerator cavity. The magnitude of the electric field of the confined mode is shown in color. The mode structure resembles the structure of the  $TM_{010}$  mode of a conventional linac pillbox cavity.

The MIT PBG gyrotron resonator cavity is made up of a triangular lattice of 102 copper rods and operates in a TE mode at 140 GHz [8]. Although the triangular array can hold 121 rods, but the 19 innermost rods were omitted to create a defect. The lattice parameters are: the post radius  $a = 0.795$  mm and the distance between the nearest posts



$b = 2.03$  mm, which corresponds to  $a/b = 0.39$  and  $\omega b/c = 5.95$ . The operational point of the cavity is shown by the solid dot in Fig. 8(b). It can be seen from the picture, that the cavity operates in the middle of the first-order global band gap. The HFSS model of the PBG gyrotron cavity is shown in Fig. 11(b) with the magnitude of the electric field in the confined mode shown in color. The mode structure resembles the structure of the  $TE_{041}$  mode of a conventional gyrotron cavity.

The PBGSS code calculations not only help us with understanding of the former experimental results, but also suggest some improvements, which can be made in future cavity designs. For example, as it can be seen from Fig. 5(b), the post radius in the accelerator cavity at 17 GHz can be increased without affecting the selectivity properties. The increase of the post radius can help to solve the problem of the rods cooling, which becomes critical in high intensity rf accelerators.

## VI. CONCLUSIONS

We conducted an extensive computational investigation of 2D metallic photonic band gap structures with application to the design of vacuum electron devices and rf accelerators. A finite-difference code was developed to study the bulk wave propagation properties in the PBG structures. Two types of metal post lattices, namely, square and triangular, were considered. We computed the dispersion characteristics for both TE and TM modes and determined the global TE and TM band gaps. Striking differences were found between the band gap structures in metallic lattices and those in dielectric lattices, especially for TM modes.

An attempt was made to check the validity of the calculations theoretically. The simplest limit is when the radii of the lattice posts are much smaller than the wavelength and the distance between the posts. In this limit the approximate dispersion relations were derived in the framework of a quasistatic approach. We compared the approximate dispersion curves with the results of the PBGSS calculations and found good agreement. We also explained the logarithmic behavior of the width of the local bandgap at the X point when  $a/b \rightarrow 0$ . Further development of the quasistatic theory is under way in order to find an explanation for some other features of the dispersion curves.

Finally, the results of the global band gap calculations were compared with two PBG experiments conducted at MIT. The results of the calculations on the global band gaps not only allowed us to understand better the experimental results but provided us with useful information for future PBG cavity designs.

## **ACKNOWLEDGEMENTS**

This work was supported in part by the Department of Defense under the MURI Innovative Microwave Vacuum Electronics Program, 1999, and in part by the Department of Energy, office of High Energy and Nuclear Physics. Research by C. Chen was also supported by the Air Force Office of Scientific Research, Grant No. F49620-00-1-0007. The authors wish to thank V. Khemani for his assistance in the development of the PBGSS code. We also acknowledge helpful discussions with Winthrop Brown and Mark Hess, and with Profs. Michael I. Petelin and Nikolay F. Kovalev (IAP RAS).

## REFERENCES

1. E.Yablonovitch, T.J.Gmitter, and K.M.Leung, Phys. Rev. Lett. **67**, 2295 (1991).
2. J.D.Joannopoulos, R.D.Meade, and J.N.Winn, *Photonic Crystals: Molding the Flow of Light* (Princeton Univ. Press, Princeton, 1995).
3. F.-R. Yang, K.-P. Ma, Y. Qian, and T. Itoh, IEEE Trans. MTT **48**, 2092 (1999).
4. J.A. Higgins, M. Kim, J.B. Hacker, D. Sievenpiper, IEEE Trans. MTT **48**, 2139 (1999).
5. D.R.Smith, S.Schultz, N.Kroll, M. Sigalas, K.M. Ho, and C.M. Soukoulis, Appl. Phys. Lett. **65**, 645 (1994).
6. D.R. Smith, N. Kroll, and S. Schultz, in *Advanced Accelerator Concepts*, AIP Conference Proceedings **398**, 761 (AIP, New York, 1995).
7. M.A. Shapiro, W.J. Brown, I. Mastovsky, J.R. Sirigiri, and R.J. Temkin, Phys. Rev. Special Topics: Accelerators and Beams **4**, 042001 (2001).
8. J. R. Sirigiri, K.E. Kreischer, J. Machuzak, I. Mastovsky, M. A. Shapiro, and R. J. Temkin, Phys. Rev. Lett. **86**, 5628 (2001).
9. P. R. Villeneuve and M. Piche, Phys. Rev. **B46**, 4973 (1992).
10. H.-Y.-D. Yang, IEEE Trans. MTT **44**, 2688 (1996).
11. C.M. Anderson and K.P Giapis, Phys. Rev. Lett. **77**, 2949 (1996).
12. T. Suzuki and P.K.L. Yu, Phys. Rev. **B57**, 2229 (1998).
13. N.A. Nicorovici, R.C. McPhedran, and L.C. Botten, Phys. Rev. **E52**, 1135 (1995).
14. M. Qiu and S. He, J. Appl. Phys **87**, 8268 (2000).
15. J. H. Billen and L. M. Young, POISSON SUPERFISH, Los Alamos National Laboratory, Report LA-UR-96-1834 (1996).
16. Ansoft High Frequency Structure Simulator – User’s Manual, Ansoft Corp (1999).
17. E.I. Smirnova and C. Chen, “*Global photonic band gaps in two-dimensional metallic lattices*,” Phys. Rev. Lett., Submitted for publication (May, 2001).
18. E.I. Smirnova and C. Chen, *Photonic Band Gap Structure Simulator, User’s Manual, Version 1.0* (June, 2001, unpublished).
19. *Waveguide Handbook*, ed. N.Marcuvitz, (Boston Technical Publishers, 1964).

## FIGURE CAPTIONS

Fig. 1. Scheme of PBG structures representing (a) square lattice and (b) triangular lattice of perfectly conducting cylinders with radius  $a$  and spacing  $b$ .

Fig. 2. Reciprocal lattices and Brillouin zones for (a) square lattice and (b) triangular lattice (irreducible Brillouin zones for each type of lattice are shaded).

Fig. 3. Plots of the normalized frequency  $\omega b/c$  versus normalized wave number for the first and second TM propagating modes as obtained from PBGSS calculations,  $a/b = 0.2$ . The solid curve represents the first TM propagating mode, and the dashed curve represents the second TM propagating mode. The two cases correspond to (a) wave propagation in the  $x$ -direction with  $k_y = k_z = 0$  through the square lattice, and (b) wave propagation in the  $y$ -direction with  $k_x = k_z = 0$  through the triangular lattice.

Fig. 4. Plots of the several lowest normalized eigenmodes versus the wave vector  $\mathbf{k}_\perp$  for TM modes as  $\mathbf{k}_\perp$  varies from the center of the Brillouin zone ( $\Gamma$  point in Fig. 2), to the nearest edge of the Brillouin zone (X point in Fig. 2), and to the far edge of the Brillouin zone (M or J point). Here,  $a/b = 0.2$ , and the two cases correspond to (a) square lattice and (b) triangular lattice.

Fig. 5. Plots of global frequency band gaps for TM mode as functions of  $a/b$  as obtained from PBG calculations for (a) square lattice and (b) triangular lattice. The solid dot represents the operating point of the 17GHz MIT accelerator cavity.

Fig. 6. Plots of the normalized frequency  $\omega b/c$  versus normalized wave number for the first and second TE propagating modes as obtained from PBGSS calculations,  $a/b = 0.2$ . The solid curve represents the first TE propagating mode, and the dashed curve represents the second TE propagating mode. The two cases correspond to: (a) wave propagation in the  $x$ -direction with  $k_y = k_z = 0$  through the square lattice, and (b) wave propagation in the  $y$ -direction with  $k_x = k_z = 0$  through the triangular lattice.

Fig. 7. Plots of the several lowest normalized eigenmodes versus the wave vector  $\mathbf{k}_\perp$  for TE modes as  $\mathbf{k}_\perp$  varies from the center of the Brillouin zone ( $\Gamma$  point in Fig. 2), to the nearest edge of the Brillouin zone (X point in Fig. 2), and to the far edge of the Brillouin

zone (M or J point). Here,  $a/b = 0.2$ , and the two cases correspond to (a) square lattice and (b) triangular lattice.

Fig. 8. Plots of global frequency band gaps for TE mode as functions of  $a/b$  as obtained from PBG calculations for (a) square lattice and (b) triangular lattice. The solid dot represents the operating point of the 140GHz MIT gyrotron cavity.

Fig. 9. Equivalent circuit model for wave propagation in the  $x$ -direction in the square lattice: a) geometry and b) equivalent circuit for one row of posts.

Fig. 10. Comparison between the PBGSS calculations and quasistatic estimates of the local TM band gap width at  $\mathbf{k} = (\pi/b, 0, 0)$  for the square lattice.

Fig. 11. The relative magnitude of the electric field in a mode confined in PBG cavity as obtained from the HFSS simulations for (a)  $TM_{010}$ -like mode at 17 GHz, and (b)  $TE_{041}$ -like mode at 140 GHz.

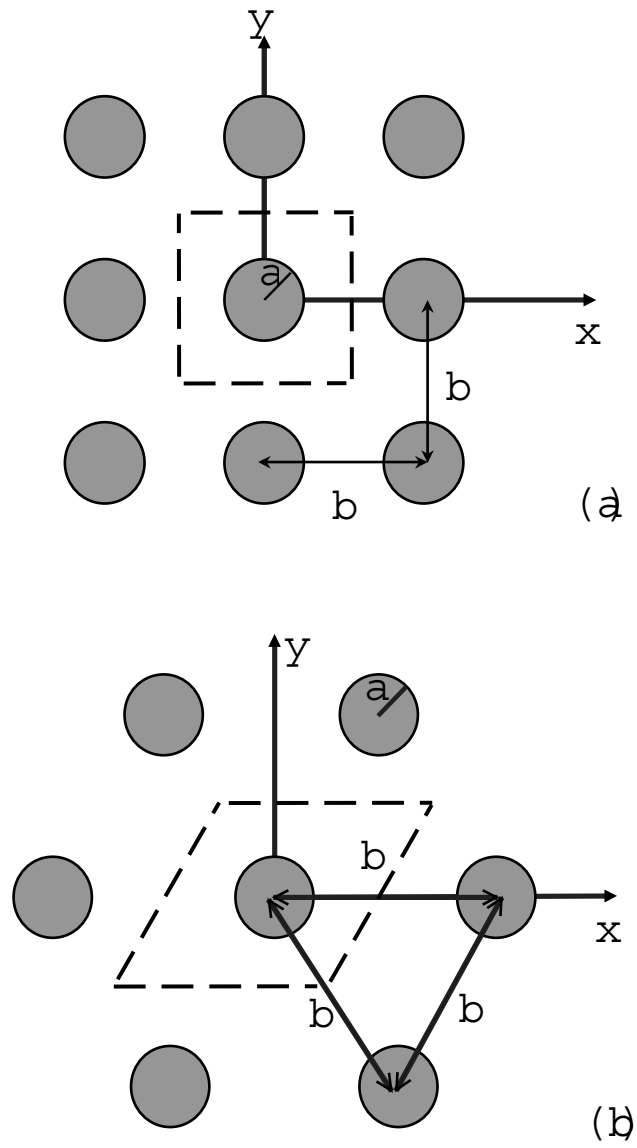


Fig. 1.

E.I. Smirnova et al.  
 J. Appl. Phys.

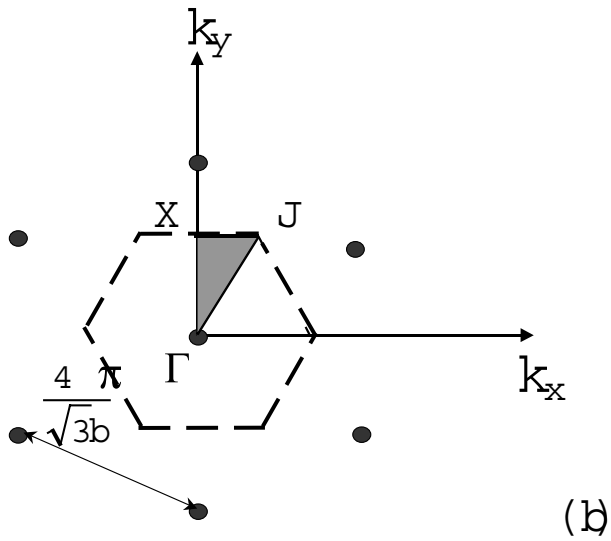
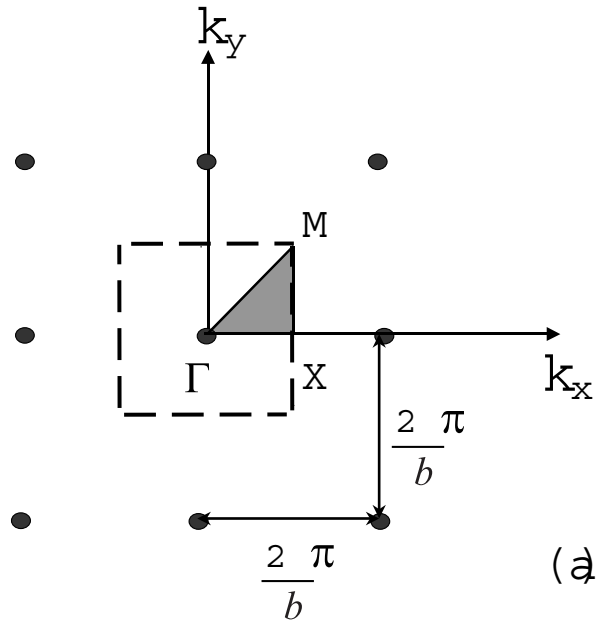


Fig. 2.

E.I. Smirnova et al.

J. Appl. Phys.



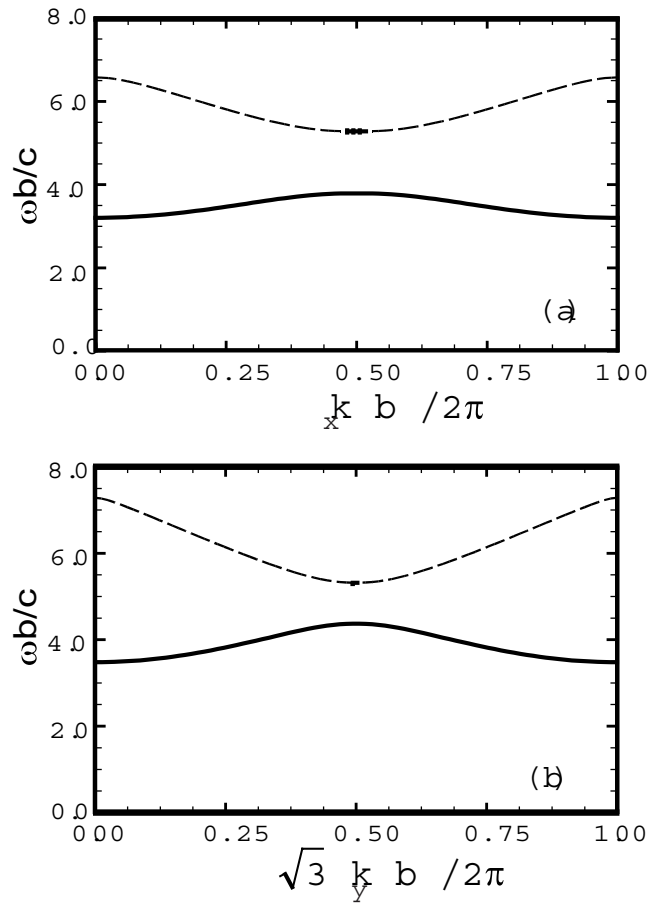


Fig. 3.

E.I. Smirnova et al.  
 J. Appl. Phys.

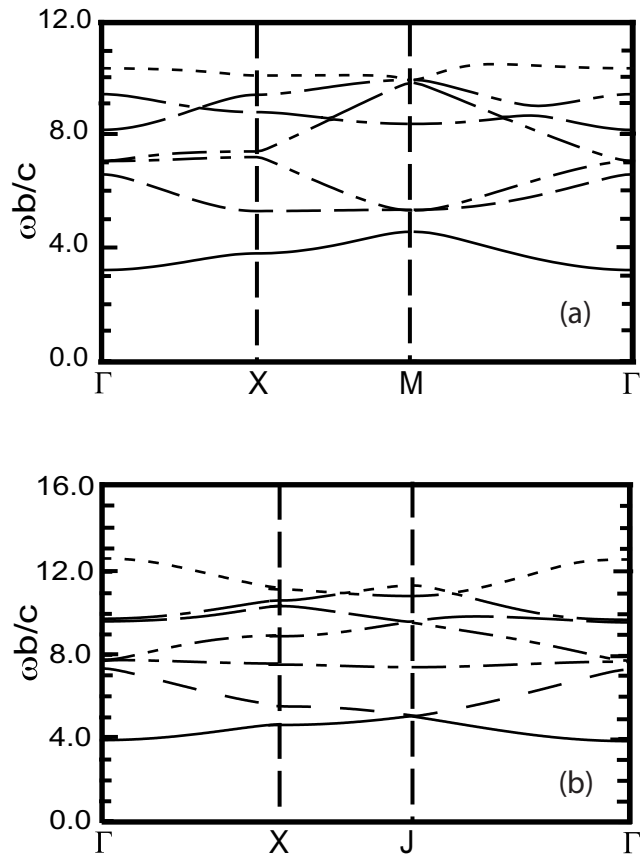


Fig. 4.

E.I. Smirnova et al.

J. Appl. Phys.

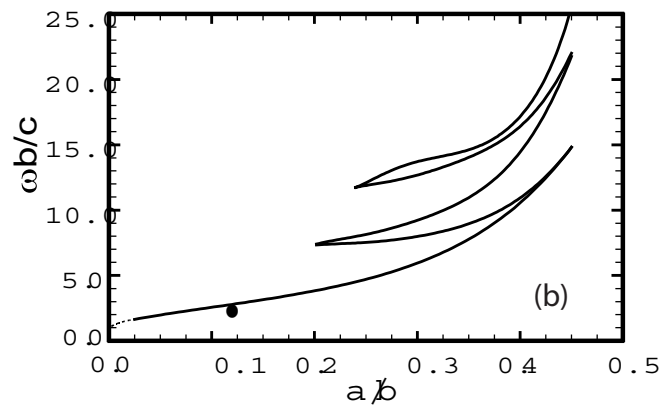
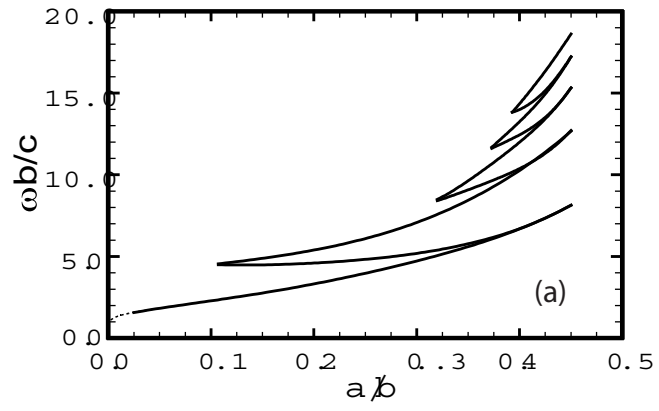


Fig. 5.

E.I. Smirnova et al.  
J. Appl. Phys.

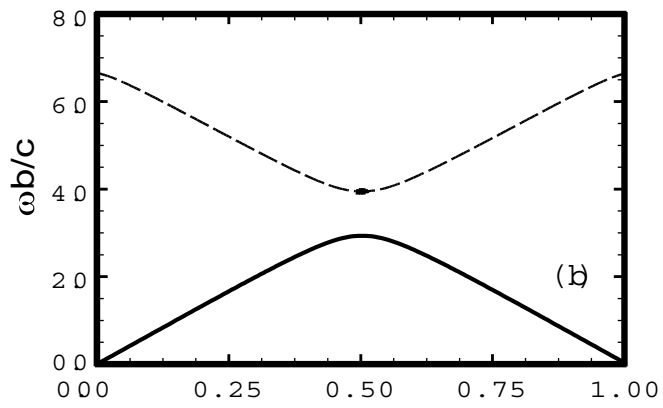
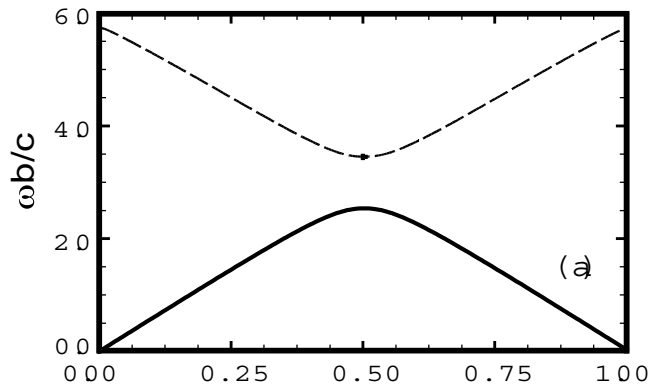


Fig. 6.

E.I. Smirnova et al.

J. Appl. Phys.

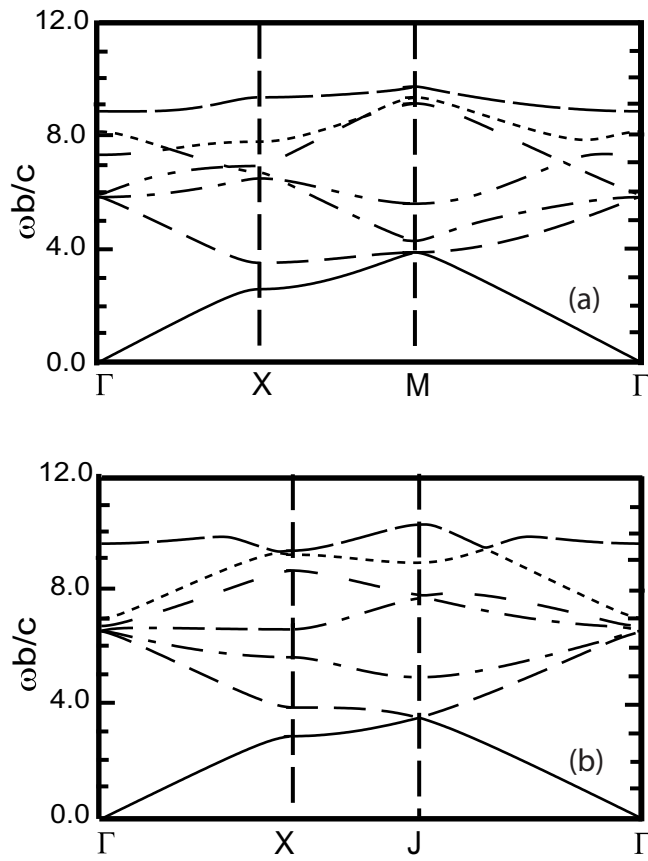


Fig. 7.

E.I. Smirnova et al.  
 J. Appl. Phys.

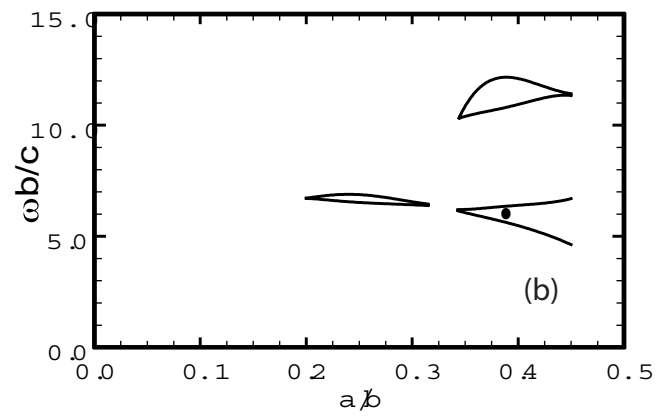
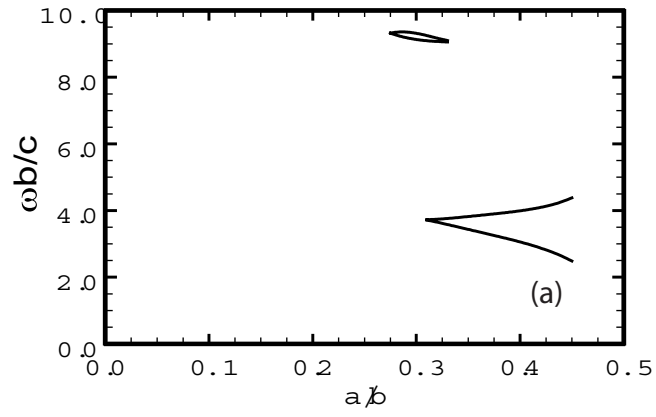


Fig. 8.

E.I. Smirnova et al.

J. Appl. Phys.

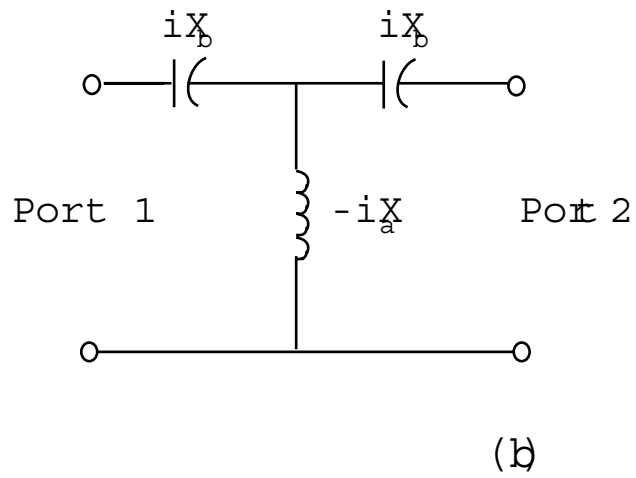
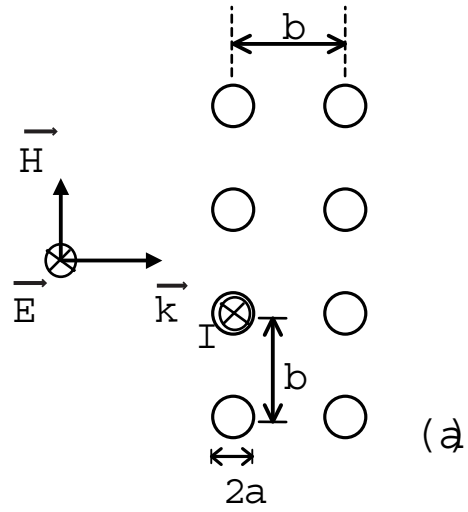


Fig. 9.

E.I. Smirnova et al.

J. Appl. Phys.

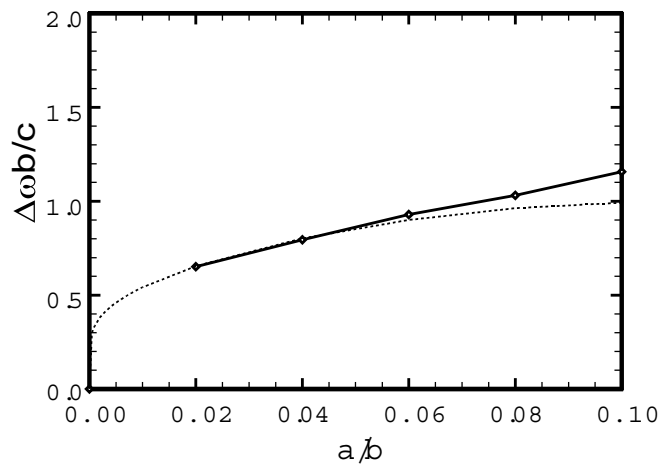


Fig. 10.

E.I. Smirnova et al.

J. Appl. Phys.



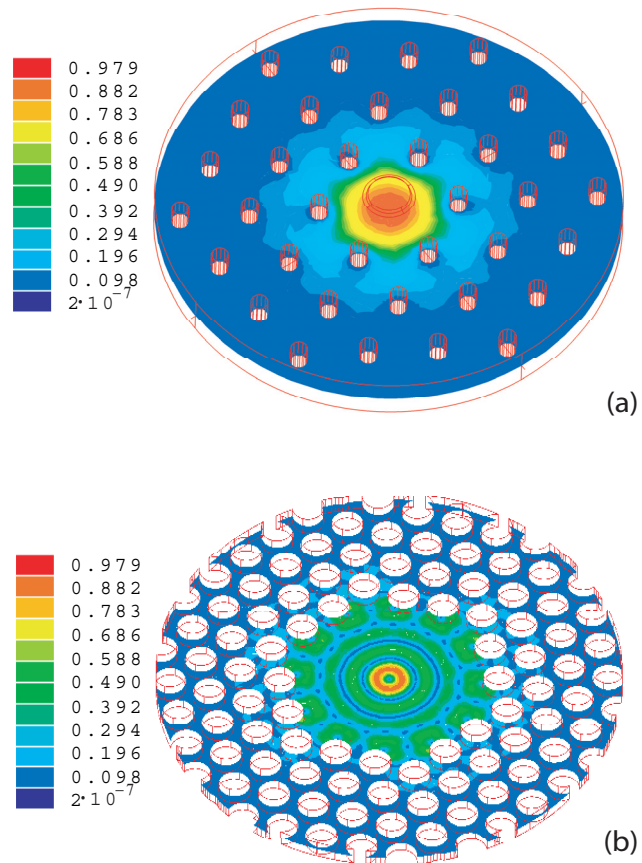


Fig. 11.

E.I. Smirnova et al.  
 J. Appl. Phys.